Earth and Planetary Science Letters 396 (2014) 88–96

Contents lists available at ScienceDirect

Earth and Planetary Science Letters

www.elsevier.com/locate/epsl

Probing the lithospheric rheology across the eastern margin of the Tibetan Plateau

Mong-Han Huang [a,*], Roland Bürgmann [a], Andrew M. Freed [b]

[a] Department of Earth and Planetary Science, University of California, Berkeley, CA, 94720-4767, USA
[b] Department of Earth, Atmospheric, and Planetary Sciences, Purdue University, West Lafayette, IN, 47907, USA

ARTICLE INFO

Article history:
Received 3 February 2014
Received in revised form 22 March 2014
Accepted 1 April 2014
Available online xxxx
Editor: P. Shearer

Keywords:
lithospheric rheology
2008 Wenchuan earthquake
postseismic deformation
geodesy
finite element modeling

ABSTRACT

The fundamental geological structure, geodynamics, and rheology of the Tibetan Plateau have been debated for decades. Two end-member models have been proposed: (1) the deformation of Tibet is broadly distributed and associated with ductile flow in the mantle and middle or lower crust, (2) the Tibetan Plateau formed during interactions between rigid lithospheric blocks with localization of deformation along major faults. The nature and distribution of continental deformation are governed by the varying rheology of rocks and faults in the lithosphere. Insights into lithospheric rheology can be gained from observations of postseismic deformation, which represents the response of the Earth's interior to coseismic stress changes. Here we use up to 2 years of InSAR and GPS measurements to investigate postseismic displacements following the 2008 M_w 7.9 Wenchuan earthquake in eastern Tibet and probe the differences in rheological properties across the edge of the Plateau. We find that near-field displacements can be explained by shallow afterslip on the Beichuan Fault, which is anti-correlated with the coseismic slip distribution. Far-field displacements cannot be explained by a homogeneous rheology, but instead require a viscoelastic lower crust (from 45 to 60 km depth) beneath Tibet with an initial effective viscosity of 4.4×10^{17} Pa s and a long-term viscosity of 10^{18} Pa s, whereas the Sichuan Basin block has a high-viscosity upper mantle ($>10^{20}$ Pa s) underlying an elastic 35-km-thick crust. The inferred strong contrast in lithospheric rheologies between the Tibetan Plateau and the Sichuan Basin is consistent with models of ductile lower crustal flow that predict maximum topographic gradients across the Plateau margins where viscosity differences are greatest.

1. Introduction

The Himalayan–Tibetan orogen is a classic example of continent–continent collision resulting in a series of active mountain ranges, starting ~50 million years ago (Thatcher, 2009; Royden et al., 2008; Tapponnier et al., 2001). The tectonic evolution and geodynamics of the Tibetan Plateau, with its average elevation of ~5 km and 60-to-80-km-thick crust, continue to be topics of debate. In the east, the Tibetan Plateau has collided with the Sichuan Basin since the Miocene and produced the Longmen Shan and its great topographic relief, rising ~6 km over the Sichuan Basin within less than 40 km horizontal distance (Hubbard et al., 2010). The low-lying Sichuan Basin is roughly circular, and seismic tomography suggests that a thick, cold mantle lithosphere underlies a 35-km-thick crust with ~10 km of mostly undeformed Mesozoic and Paleozoic sediments (Li et al., 2009). From east to west, the Pengguan fault (PGF) and the Beichuan fault (BCF) are the two major active northwest dipping fault zones of the Longmen Shan (Fig. 1) and represent reactivations of Mesozoic fold-and-thrust structures (Burchfiel et al., 2008). The interseismic deformation across the Longmen Shan amounts to <3 mm/yr shortening with an oblique right-lateral shear component (Shen et al., 2005, 2009). Though many geophysical and geological studies have been carried out in eastern Tibet, the rheology of the lower crust and upper mantle is poorly constrained. Thus, the nature of the mountain building process and style of deep-seated deformation of eastern Tibet continue to be unresolved (Burchfiel et al., 2008).

On 12th May, 2008, the M_w 7.9 Wenchuan earthquake occurred along the eastern Longmen Shan and caused more than 80,000 fatalities. The earthquake ruptured ~235 km of the BCF and the entire PGF (Shen et al., 2009; Qi et al., 2011). Several coseismic slip models have been proposed from seismic, geodetic, or combined inversions (Zhang et al., 2010). All of the slip models show oblique thrusting along the southwestern BCF and a right-lateral slip component that gradually increases towards the northeastern end of the BCF (Fig. 1). The inferred deep geometry of the PGF and

* Corresponding author. Tel.: +1 510 612 7241.
E-mail address: mong@berkeley.edu (M.-H. Huang).

http://dx.doi.org/10.1016/j.epsl.2014.04.003
0012-821X/

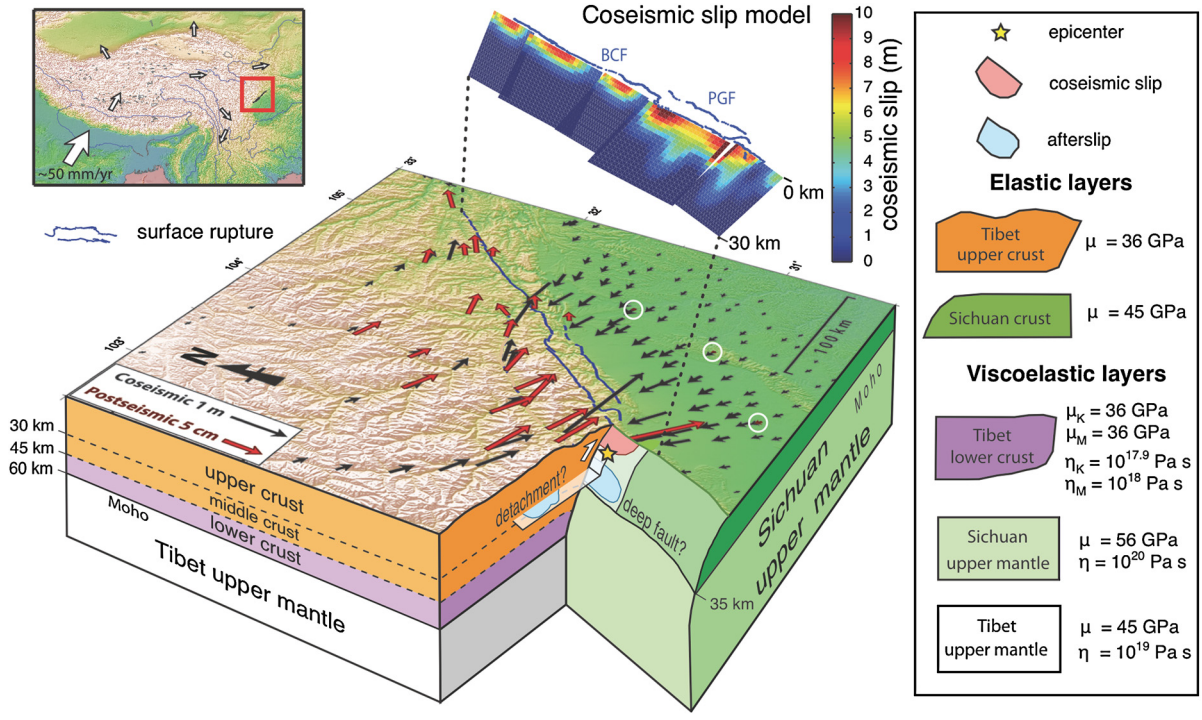

Fig. 1. Three-dimensional representation of eastern Tibet. The upper left map shows the Tibetan Plateau, and the red square indicates the study area. The black and red arrows in the 3D block diagram are the co- and estimated first year postseismic GPS measurements. The white circles in the Sichuan Basin show stations that have <5 mm postseismic measurements. The detachment and deep faults are based on Shen et al. (2009) and Qi et al. (2011). The coseismic slip model is based on inversion of the coseismic GPS displacements. The rheologic properties of the viscoelastic relaxation model are given in the legend. (For interpretation of the references to color in this figure legend, the reader is referred to the web version of this article.)

BCF, either shallowing into a sub-horizontal detachment (Hubbard et al., 2010) or a more steeply dipping localized shear zone to the Moho (Guo et al., 2013), is tested by coseismic slip models (Zhang et al., 2010). Some rupture models prefer a moderate amount of coseismic slip on a shallowly-dipping detachment fault extending downdip below ~20 km depth (Shen et al., 2009; Qi et al., 2011; Zhang et al., 2010).

The redistribution of stresses by the earthquake induce a variety of postseismic processes that result in observable surface displacements, which can then be used to constrain the rheologic properties of rocks and faults deep beneath the surface (Bürgmann and Dresen, 2008). Postseismic mechanisms include aseismic afterslip, aftershocks, viscoelastic relaxation in the lower crust and/or upper mantle, and poroelastically induced fluid flow. The contributions from these mechanisms to observed postseismic deformation can, however, be difficult to separate, hence a major challenge lies in resolving the contributions of various postseismic processes to the observed transient surface deformation (Hearn, 2003). In this study, we incorporate two years of geodetic measurements after the Wenchuan earthquake and numerical modeling to isolate the individual contributions and use these constraints to probe the deep rheology of eastern Tibet and the adjoining Sichuan Basin.

2. Data

2.1. GPS

The GPS postseismic displacement data are from Shen et al. (2009) and Ding et al. (2013). Both studies fit the early GPS horizontal data with a logarithmic function: $D(t) = D_{x,y}\ln(1 + t/\tau)$, where $D_{x,y}$ is the amplitude of the postseismic displacement of each component. The logarithmic relaxation times (τ) of the functions are 8 and 38 days for Shen et al. (2009) and Ding et al. (2013), respectively. There are 37 stations from Shen et al. (2009) and 16 stations from Ding et al. (2013). To compute the 1-year postseismic displacement, we use the amplitude terms ($D_{x,y}$) of each station and set $t = 365.25$ days.

2.2. InSAR and PSInSAR

We use Advanced Land Observation Satellite (ALOS) PALSAR L-band (23.6 cm) data from the Japan Aerospace Exploration Agency and Envisat ASAR C-band (5.6 cm) from the European Space Agency to observe the postseismic deformation starting a month after the mainshock until about 1.5 years afterward. The line-of-sight incidence angle at the center of the image track is ~35° for ALOS and ~23° for Envisat. There are up to 26 ALOS acquisitions from tracks 471–475 during the postseismic period, but the spatial baselines between acquisitions are often too large for producing interferograms (>1500 m), due to the orbital drift of the ALOS satellite (Supplementary Information S1). The selected interferograms are mostly 1.5–2 year pairs, similar to the period of the orbital drift. There are no SAR acquisitions of Envisat after April of 2012 and ALOS after April of 2011 due to the ends of the missions. All of the ALOS and Envisat acquisitions are from ascending and descending orbits, respectively (Supplementary Tables S1 and S2). All SAR interferograms are generated using ROI_PAC 3.0 (Rosen et al., 2004). The 90 m Shuttle Radar Topography Mission (SRTM) DEM is used to correct the phase due to topography. Snaphu 1.4.2 (Chen and Zebker, 2002) is used for the phase unwrapping.

3. The Wenchuan postseismic displacement

The GPS measurements of deformation following the Wenchuan earthquake show an overall NW-SE convergence along the southern BCF, transitioning into right-lateral strike-slip motion along the northern BCF (Fig. 1, data based on Shen et al., 2009 and Ding et al., 2013). The first-order patterns of the co- and postseismic

displacements are similar (Fig. 1), but the peak postseismic motions occur about 40 km NW from the greatest coseismic displacement, which is located at the surface rupture (Shen et al., 2009). Compared with the coseismic deformation, the spatial wavelength of the postseismic deformation is much greater, suggesting either deep-seated afterslip or viscoelastic relaxation in the deeper parts of a thick lower crust or upper mantle. In the footwall (to the SE of the fault), most of the displacements in the Sichuan Basin are toward the NW, but with much smaller amplitude (<5 mm in the first year) than in the hanging wall (Fig. 1).

Thirty-three ascending ALOS PALSAR acquisitions from tracks 471 to 475 cover the entire Wenchuan postseismic area (Supplementary Table S1). The 1–2 year SAR interferograms (Fig. 2) show both near- and far-field postseismic deformation along the Longmen Shan. A sharp change in the line-of-sight (LOS) displacement appears across the northern BCF (Fig. 2c). This range change is consistent with shallow right-lateral strike slip of ~3 cm in the first year (profile BB′ in Fig. 2c). However, the full extent of creep on the northern BCF is unclear due to ionospheric and tropospheric noise that affects the interferograms (Supplementary Fig. S1a). Along the southern BCF (Fig. 2b), there is no sharp range change across the surface rupture, but a ~50-km-wide zone of range decrease extends from the PGF across the Longmen Shan (profile AA′ in Fig. 2b). Due to low signal-to-noise levels and strong atmospheric perturbations (Supplementary Information S1), we choose to exclude the ALOS measurements as model constraints.

Fifteen Envisat ASAR acquisitions of descending track 290 are used to generate time series of postseismic displacement in the southern Longmen Shan (Supplementary Table S2). The small baseline subset (SBAS) method (see Supplementary Information S2) is used to generate InSAR time series from June, 2008 to December, 2009. The result (Fig. 3a) shows a zone of range decrease of more than 10 cm in the southern Longmen Shan about 30–100 km NW of the surface rupture (green to red color in Fig. 3a). Time series of four selected groups of pixels illustrate the postseismic displacement in the near-, mid-, and far field of the hanging wall and footwall blocks (black lines in Fig. 3c). In eastern Tibet, the near- and mid-field measurements (2 and 3 in Fig. 3c) show a rapidly decaying trend, accumulating up to 12 cm of range decrease in 1.5 years. On the Sichuan Basin, the data show mostly insignificant range change. There is evidence for nearly 1 cm of subsidence near Chengdu (1 in Fig. 3c), but the range increase rate is not consistent over time and seems to have a seasonal variation during the 1.5-year period.

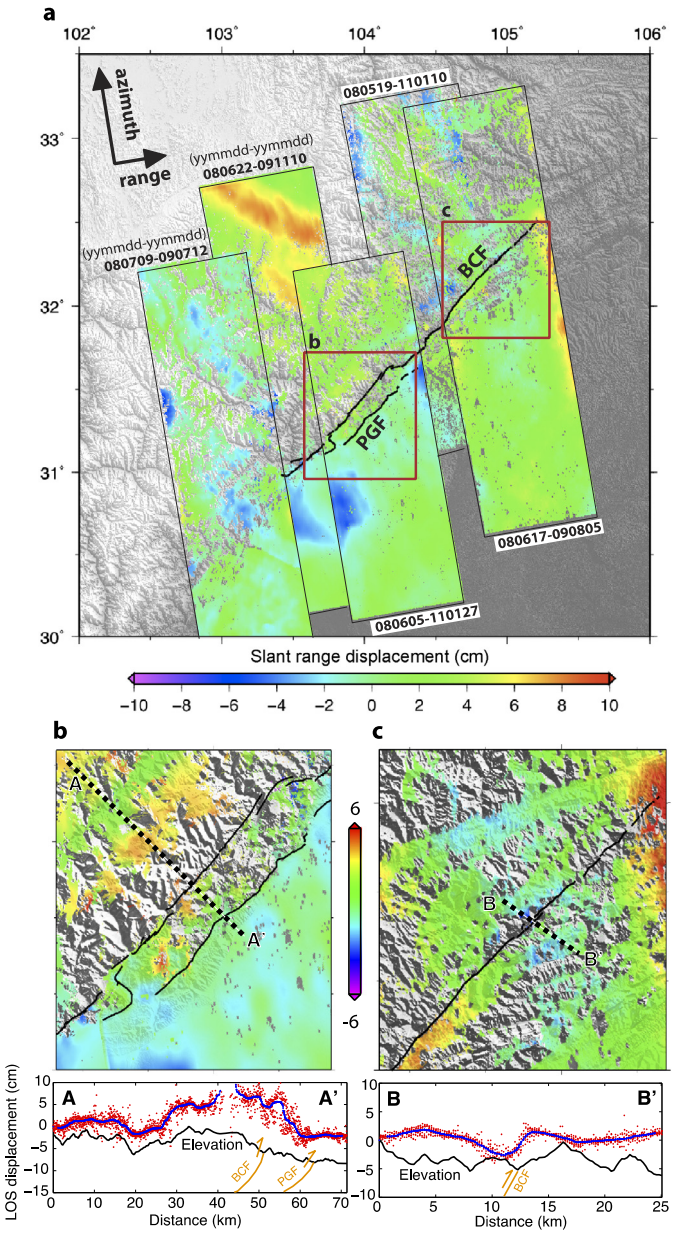

Fig. 2. ALOS PALSAR 2-year postseismic displacement. **(a)** Interferograms of five ascending tracks (T471–475) showing about 2-year postseismic displacement (acquisition dates are shown above or below the interferograms, see Supplementary Table S1 for a list of the interferograms). Warm and cold colors show range shortening and lengthening, respectively. The average look angle of ALOS at the center of the image track is ~35°. **(b)** Close-up view of the SW section of the surface rupture. **(c)** Close-up view of the NE BCF. The profiles below **(b)** and **(c)** show the elevation and the LOS displacement during the acquisitions. The black lines are the elevation and the red dots are the LOS displacements within 5 km along the profile. The blue lines are the mean LOS displacement. (For interpretation of the references to color in this figure legend, the reader is referred to the web version of this article.)

4. Modeling approach

Shao et al. (2011) used the first 14 days of postseismic near-field GPS data to conclude that both afterslip and viscoelastic relaxation contributed to the deformation transients. Here we test models of these processes, as well as poroelastic rebound, constrained by one-year GPS displacements and 1.5-year Envisat time series.

4.1. Afterslip models

Afterslip describes the process when predominantly aseismic fault slip occurs on or beneath the rupture zone, in the days to years after the main shock. We consider inverse dislocation models with afterslip on either a straight down-dip extension of the coseismic rupture (Guo et al., 2013), or on a shallowly dipping detachment (Hubbard et al., 2010; Shen et al., 2009; Qi et al., 2011). To evaluate if afterslip distributions found in the kinematic inversions are mechanically plausible, we also compute the distribution of afterslip from a model of slip on a friction-free fault driven by the coseismic stress changes. Such a stress-driven model predicts the maximum afterslip that can be expected based on the moment release of the earthquake.

The distributed slip models are calculated by the inversion of geodetic data (GPS and InSAR) for slip on a discretized dislocation model. We use the coseismic GPS data from Qi et al. (2011) and postseismic GPS and InSAR data for co- and post-seismic inversions. The geodetic Green's functions are computed using the programs EDGRN/EDCMP (Wang et al., 2006) for the coseismic and afterslip inversions. This allows for the calculation of the Green's functions relating unit slip on each subfault dislocation to surface displacements in a layered elastic model over a half-space. The

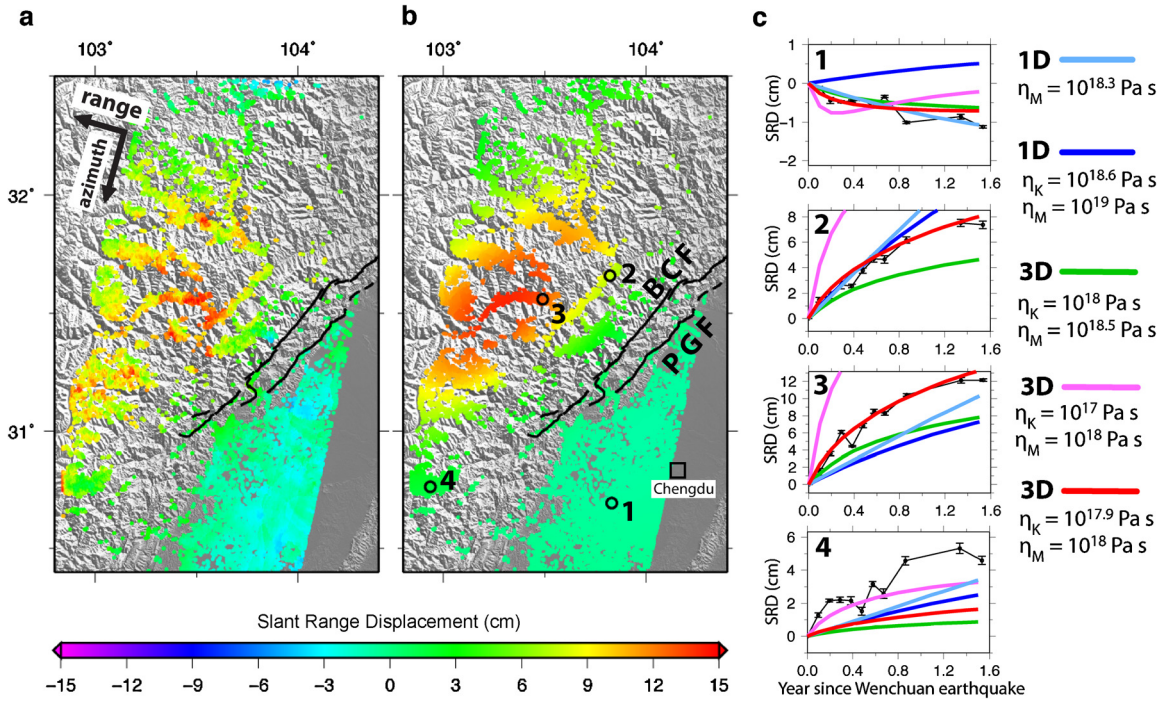

Fig. 3. 1.5-year postseismic displacement from Envisat InSAR data. **(a)** The stable image points extracted with the SBAS algorithm (Supplementary Information S2) and the color represents the cumulative slant-range displacement. Warm colors indicate range shortening. The average look angle of Envisat at the center of the image track is ∼23°. **(b)** The predicted InSAR displacement from the preferred viscoelastic relaxation model. **(c)** Selected InSAR slant-range displacement (SRD) time series (black lines) at labeled points shown in **(a)** and predicted time series (red lines) based on the viscoelastic relaxation model in **(b)**, as well as selected 1D and 3D model results. (For interpretation of the references to color in this figure legend, the reader is referred to the web version of this article.)

weight between GPS and InSAR is chosen so that both datasets have similar variance reduction (see Huang et al., 2013 for detail about data weighting and smoothing factors). We use the eastern Tibet elastic structure from Li et al. (2011) to compute the Green's functions for the afterslip model. For the deep fault geometry, we keep the fault dip angle the same as Shen et al. (2009) and extend the fault width so it can reach the Moho depth (about 60 km) as the deepest location of afterslip. We also consider a fault geometry with a wide, shallowly dipping detachment fault 25–30 km below the Longmen Shan based on Qi et al. (2011).

4.2. Viscoelastic relaxation

Viscoelastic forward models explore the rheologic structure required to explain postseismic observations if they were driven solely by viscoelastic relaxation of coseismic stresses imparted to the lower crust and mantle. We also consider a multiple-mechanism model in which we first solve forward models of viscoelastic relaxation, then invert for a companion afterslip component required to satisfy the remaining displacement residuals.

We initially consider a 1D-layered structure (Pollitz, 1992) that is composed of two viscoelastic layers (lower crust and upper mantle) below an elastic lid representing the upper crust, with a crustal thickness of 60 km (Zhang et al., 2009b). The shear moduli of the layers are estimated from regional shear-wave tomography models (Li et al., 2009; see Fig. 1). We evaluate a series of forward models to achieve a best fit to the Envisat time series and 1-year GPS displacements by varying the thickness and viscosity of the lower crust. The viscosity of the upper mantle is based on a series of tests varying viscosity from 10^{18} to 1^{20} Pa s, and is determined to be at least 10^{19} Pa s. The mantle viscosity is poorly constrained because the coseismic stress change below the Moho (>60 km) is too small to produce significant relaxation.

We use the finite element model code Abaqus 6.12 (http://www.simulia.com/products/abaqus_fea.html) to construct a 3D geologic structure to better represent the lateral heterogeneity between eastern Tibet and the Sichuan Basin. This model extends 1600 km in the horizontal dimension with the coseismic surface rupture at the center, and vertically to a depth of 1000 km (Fig. 5a and b), so the fixed boundaries do not significantly affect the coseismic stress change and the relaxation. The fault geometry and the coseismic slip distribution are based on Shen et al. (2009) with some slip adjustments to accommodate the difference between 1D homogeneous and 3D heterogeneous models. Seismic tomography (Li et al., 2009) and receiver function studies (Zhang et al., 2009a) inform the first-order geologic structure. On the Sichuan side, the entire 35-km-thick crust is assumed elastic overlying a viscoelastic upper mantle. On the Tibetan side, the upper crust (0–30 km) is elastic. We assume that either the middle (30–45 km) or the lower (45–60 km) crust is viscoelastic (Fig. 5b), and we vary the viscosity for either layer to fit the geodetic observation. Note, the middle crust is assumed elastic when considering a viscoelastic lower crust and vise versa. The viscoelastic middle crust model is to test if eastern Tibet has similar structure as a weak middle crust overlaying stronger mafic crust beneath the southern Lhasa block in southern Tibet (Nelson et al., 1996). The Tibetan upper mantle is also assumed viscoelastic.

4.3. Poroelastic rebound

Poroelastic rebound is the process in which coseismic pressure changes drive fluid flow in the crust, usually in the months following large earthquakes (Freed et al., 2006). Postseismic pore fluid flow can be driven by coseismic changes in pressure. The resulting poroelastic rebound can contribute to the postseismic surface deformation. Peltzer et al. (1996) first proposed that poroelastic rebound can explain some of the near-field postseismic displacements following the 1992 M_w 7.3 Landers, California earthquake. While evidence for poroelastic rebound is strong for some earthquakes (Peltzer et al., 1996; Jónsson et al., 2008) it has been ruled

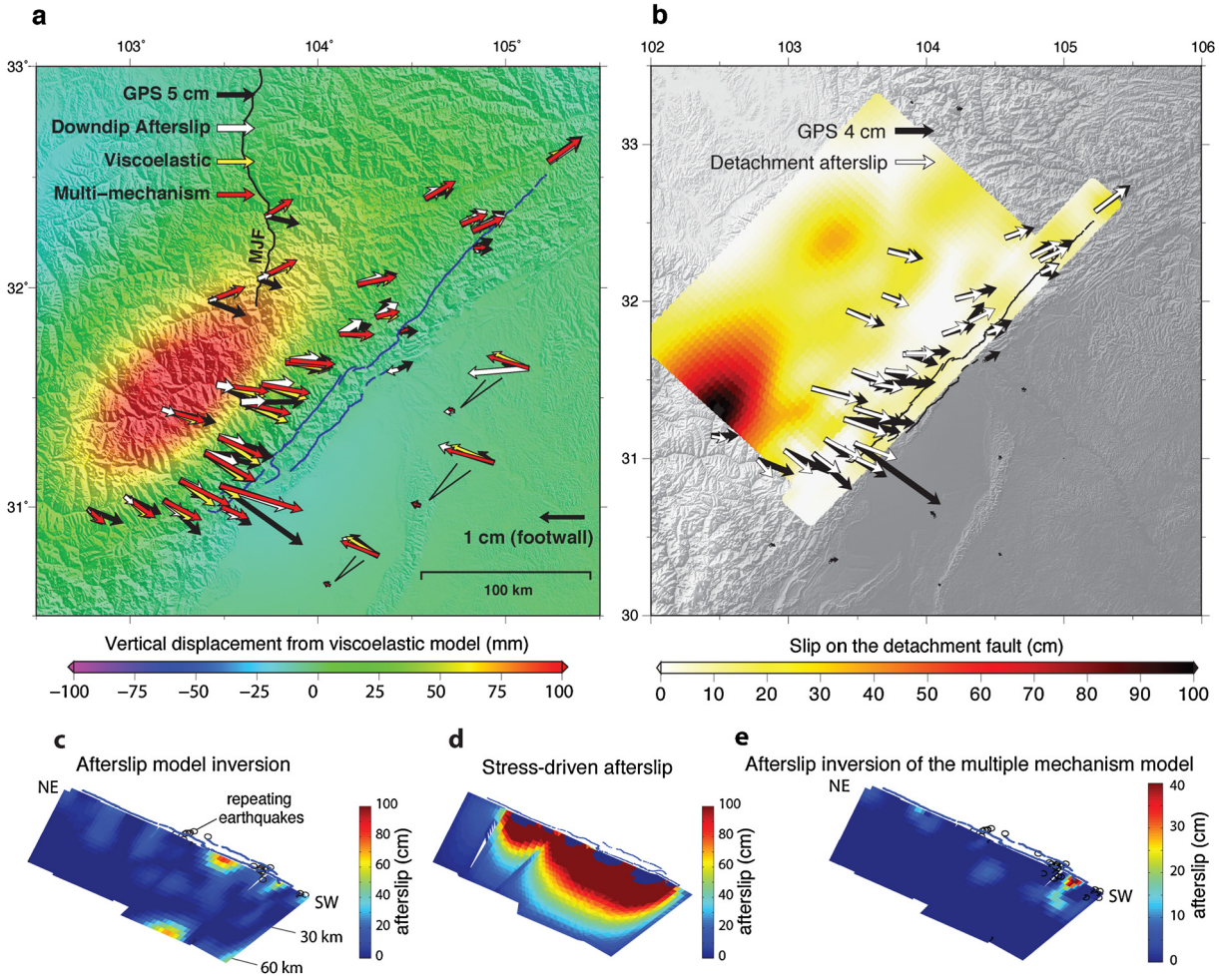

Fig. 4. Postseismic model results. **(a)** One-year postseismic GPS measurement (black arrows), modeled postseismic displacement from afterslip-only inversion (white arrows), 3D viscoelastic relaxation model (yellow arrows and vertical color contoured values), and the multiple-mechanism model (red arrows). **(b)** Afterslip distribution on the sub-horizontal detachment underneath Longmen Shan. The fault geometry is based on Qi et al. (2011). **(c)** The afterslip-only model inversion using the same fault geometry as the coseismic model but is extended to 60 km depth. Circles are repeating earthquakes (Li et al., 2011) observed from 2000 to 2008. **(d)** The stress-driven afterslip model relieving all coseismic shear-stress changes. **(e)** Afterslip distribution from the multiple-mechanism model. Note the color scale of **(c)** and **(d)** is the same. (For interpretation of the references to color in this figure legend, the reader is referred to the web version of this article.)

out in other cases (Barbot et al., 2008). Deformation from poroelastic rebound can be estimated by the transition of Poisson's ratio of the deformed volumes of rock from undrained to drained conditions after the earthquake (typically within a few months). This process represents the return of pore pressure to hydrostatic equilibrium (Peltzer et al., 1996).

5. Results

5.1. Afterslip

We use a dislocation model in an elastically layered crust to invert the observed surface motions for the optimal smoothed afterslip distribution. We modify the fault geometry proposed by Shen et al. (2009) and extend the fault down dip to 60 km depth. In the best-fitting result, there are five main slip zones in the shallower part of the fault (Fig. 4b), which are anti-correlated with the coseismic peak slip areas. The peak afterslip is 82 cm on the southern BCF near the surface. The moment released by the afterslip is 4.09×10^{19} N m (M_w 7.07), about 5.4% of the main shock based on Shen et al. (2009) and about 8.5 times of the moment released by the first year of aftershocks (M_w 6.52, based on Jia et al., 2010). Similar to the coseismic slip, the inferred afterslip is mostly oblique thrusting in the SW and right-lateral strike slip in the NE. The afterslip in the deeper sections of the fault is distributed between 30 and 60 km depth with higher (>60 cm) slip values near the bottom edge of the southern fault segments.

The fit to the geodetic measurements based on afterslip inversions is generally better in the near field (Fig. 4a). In the Tibetan far field, the afterslip model greatly underpredicts both GPS and InSAR displacements. Since the far-field displacement is directly related to the deeper slip (note the patch of deep afterslip in Fig. 4c), to improve the fit would require afterslip that extends below the Moho of eastern Tibet (i.e. greater than 60 km), well separated from the inferred region of shallow afterslip.

Alternatively, we consider a fault geometry with a shallowly dipping detachment fault 25–30 km below the Longmen Shan based on Qi et al. (2011) for the afterslip-only inversion. We use the same method as in the deep afterslip inversion (see Section 4.1). In this model, slip can extend on the detachment fault for up to ~170 km west of the coseismic surface rupture (Fig. 4b). In the best-fitting model, most of the afterslip is located in the SW part of the detachment fault, with peak amplitude of about 102 cm. This model fits the middle- to far-field horizontal GPS well, but cannot produce enough displacement in the near-field GPS and the Envisat measurements (Supplementary Fig. S3a). Peak afterslip occurs far from the rupture and coseismic stress changes. The misfit (rms for 1-year GPS and InSAR displacements) of the

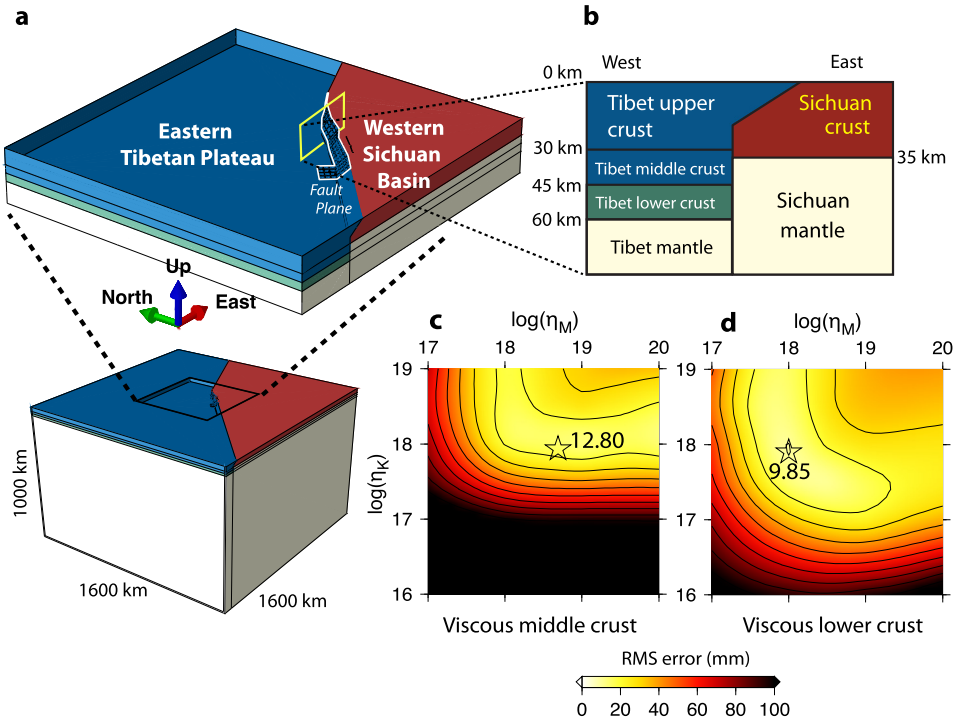

Fig. 5. **(a)** The 3D block model and the fault geometry (Shen et al., 2009) constructed using ABAQUS in regional scale and in **(b)** detail around the boundary of Tibet and Sichuan blocks. **(c)** The estimation of viscosities of Kelvin and Maxwell components of the transient Burgers-body rheology, assuming viscoelastic relaxation in Tibet's middle crust and in **(d)** Tibet's lower crust. The stars indicate the locations of the preferred model viscosities for either case, and the numbers indicate the RMS error of the best-fitting models.

detachment model is 14 mm versus 20 mm for the model inverting for afterslip on the steeper down-dip extension. The shallower (<20 km) sections of the slip models with the two fault geometries are similar. The afterslip in the multiple-mechanism model with the deep fault geometry (Fig. 4d) is located mostly in the shallower part, so the afterslip in the multiple-mechanism model with detachment fault geometry would have similar distribution as the deep fault model.

To determine whether the afterslip inversions are mechanically plausible, we examine a stress-driven frictionless afterslip model (Freed et al., 2006; Johnson et al., 2012) to estimate the maximum possible afterslip distribution assuming full relaxation of coseismic stress changes on the BCF (Supplementary Information S3). We use the same coseismic slip distribution (Fig. 1) and allow afterslip away from the rupture down to 60 km depth. As shown in Fig. 4d, the stress-driven afterslip extends to the deeper sections of the southern BCF, and includes near-surface slip where the coseismic slip is smaller. While the stress-driven afterslip greatly exceeds the inverted values in the ~10-km-wide zone below the coseismic rupture, the afterslip inversion predicts more than 50 cm of deep slip below 35 km, which exceeds the completely relaxed stress-driven afterslip of only up to 10 cm in this deep region. As a frictionless down-dip fault should enable the maximum afterslip that can be generated by coseismic stress changes, this suggests that the deep afterslip implied by the inversion is not plausible. To actually match the surface displacements with a stress driven model, it would be necessary to not allow for slip at intermediate depths, in which case even a further extended fault plane would not be able to produce a sufficient amount of deep slip.

5.2. Viscoelastic relaxation

Viscoelastic flow after a large earthquake results from the relaxation of coseismic stress changes in the lower crust and upper mantle, where high temperatures and pressures enable ductile flow of rocks (Bürgmann and Dresen, 2008). Basic viscoelastic deformation relations can be represented by equations that consider various combinations of linear elastic and linear viscous components (Bürgmann and Dresen, 2008; Wang et al., 2012). The initial 1D model composed of two Maxwell viscoelastic layers cannot predict the early fast displacements and their rapid decay in the Envisat time series (Fig. 3c). Early rapid transients are also seen in rock mechanics experiments (Chopra, 1997) and previous postseismic deformation studies (Pollitz, 2003; Ryder et al., 2007), and may reflect the transition from transient to steady-state rheologic properties following a stress perturbation. Hence, we use the bi-viscous Burgers model that is composed of a Kelvin solid (η_K) and a Maxwell fluid (η_M) to explain the two-stage displacements (Bürgmann and Dresen, 2008; Wang et al., 2012; Pollitz, 2003). The best-fitting 1D bi-viscous model (Fig. 3c) with $\eta_K = 4 \times 10^{18}$ Pa s and $\eta_M = 10^{19}$ Pa s in a layer extending from 20 to 60 km depth shows a general agreement with the observed deformation in the Longmen Shan, but fails to match the displacements in the Sichuan Basin. However, the 1D models generally predict up to 3 cm uplift and 5 cm horizontal motions in the Sichuan Basin (Supplementary Fig. S4), which greatly exceeds the geodetic observations.

The strong asymmetry of postseismic deformation across the Longmen Shan implies a rheologic contrast between the Tibetan Plateau and the Sichuan Basin. We therefore consider a 3D rheologic structure using a finite element model (Fig. 5a and b; see Section 4.2). In the Tibetan lower crust, the transient and steady-state viscosities of the crustal layers are varied from 10^{17} to 10^{20} Pa s. On the Sichuan, the upper mantle Maxwell viscosity below 35 km is allowed to vary from 10^{19} to 10^{21} Pa s. Supplementary Fig. S5 demonstrates that the upper mantle below the Sichuan Basin must have an effective viscosity above 10^{20} Pa s, as a weaker mantle produces displacements that exceed those found to the SE of the Longmen Shan. A comparison of best-fit models for relaxation in the middle or lower crust can be found in Supplementary Fig. S6

and plots of misfit as a function of transient and steady-state viscosity in the relaxing crustal layers are shown in Fig. 5c and d. The best fitting result was obtained with $\eta_K = 7.9 \times 10^{17}$ Pa s and $\eta_M = 10^{18}$ Pa s in Tibet's lower crust (i.e., initial effective viscosity $= 4.4 \times 10^{17}$ Pa s and steady-state viscosity $= 10^{18}$ Pa s; see Supplementary Information S4) and viscosity $>10^{20}$ Pa s in the upper mantle below Sichuan. This result fits the spatial and temporal pattern of the postseismic displacements well both to the NW and SE of the Longmen Shan thrust system (Figs. 3 and 4a).

5.3. Poroelastic rebound

Poroelastic rebound can be modeled as the difference between two calculated coseismic displacement fields associated with different assumed Poisson's ratios of the top 2-km-thick layer, from 0.25 (undrained) immediately following the earthquake to 0.21, representing drained conditions following fluid-pressure re-equilibration. In this model, fluid flow is assumed to occur only in the uppermost, most permeable section of the crust (Jónsson et al. 2008; Manning and Ingebritsen, 1999), but the pattern of poroelastic rebound is similar for drainage to greater depth. The coseismic input is the same as for the stress-driven afterslip model (Supplementary Information S3) and the viscoelastic relaxation models. The poroelastic rebound model with these parameters (Supplementary Fig. S2a) predicts significant near-fault displacements of up to ~4 cm in both horizontal and vertical components. However, the poroelastic rebound model cannot explain the postseismic displacement, or the misfits of afterslip and viscoelastic models (Supplementary Fig. S2b). In order to further examine the possible contribution of poroelastic rebound, we subtract the poroelastic rebound model from the observed GPS measurement, and invert for afterslip on the fault. The inverted afterslip (Supplementary Fig. S2c) is highly similar to the afterslip-only model, which implies that the poroelastic rebound model is not a significant contributor to the postseismic displacement. We rule out this mechanism as important in observed postseismic observations, as it only produces near fault displacements that are inconsistent with the observations (Supplementary Fig. S2).

6. Discussion and conclusions

6.1. Multiple mechanisms

The afterslip model (Fig. 4a and b) can explain the postseismic displacements in the near field with up to 82 cm of afterslip in the shallower (above 20 km) part of the fault. However, the fitting to the far field, especially the vertical component, requires more than 60 cm of deep afterslip below 35 km (Fig. 4c), or >1.2 m on an isolated slip zone on a horizontal detachment (Fig. 4b). On the other hand, the viscoelastic relaxation model (Figs. 3b–c and 4a) can explain middle- to far-field postseismic displacements with a 15-km-thick lower crustal layer below 45 km depth, but cannot fit the details of the near-field motions. Thus, a single mechanism cannot explain the observed postseismic displacement field. Following the exploration in the last section, we consider lower crustal relaxation of Tibet to be the main mechanism to explain the far-field measurements in eastern Tibet. If we invert the residual displacements from this model for afterslip (Fig. 4e), we find several >20 cm afterslip patches above 20 km and <10 cm afterslip deeper (25–40 km) on the southern BCF. The moment of afterslip in the multiple-mechanism is 6.56×10^{18} N m (M_w 6.54), only 16% of the moment of the afterslip-only model. The shallow model afterslip along the northern BCF can well explain the surface creep resolved in the ALOS InSAR data (Fig. 2c), as well as the near field GPS displacement along the BCF. To the northwest of the

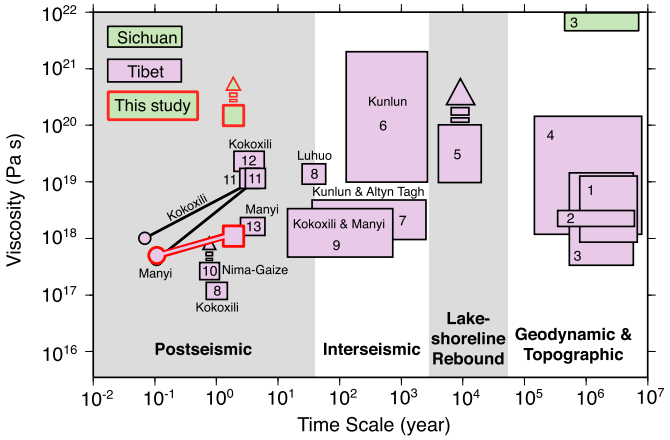

Fig. 6. Viscosity estimates of Tibet's lower crust for different time scales. The rectangles represent the range of viscosity of the lower crust estimated using constraints for different time scales. The circles represent the initial effective viscosity of a Burgers-type rheology. The arrows above the rectangles indicate that the estimated viscosity represents a lower bound. The estimated value for the Sichuan block (green square) is for the mantle below 35 km depth. The number in the rectangles refers to the cited references: 1, Beaumont et al. (2001); 2, Clark et al. (2005); 3, Cook and Royden (2008); 4, Rippe and Unsworth (2010); 5, England et al. (2013); 6, Hilley et al. (2005); 7. Hilley et al. (2009); 8, Zhang et al. (2009a); 9, DeVries and Meade (2013); 10, Ryder et al. (2010); 11, Ryder et al. (2011); 12, Wen et al. (2012); 13, Yamasaki and Houseman (2012). (For interpretation of the references to color in this figure legend, the reader is referred to the web version of this article.)

Longmen Shan close to 104°E and 32°N, none of the models accurately predict the displacement azimuths of three GPS stations (Fig. 4a). A possible cause of this misfit is triggered fault slip on the nearby Minjiang fault (MJF in Fig. 4a). Alternatively, the azimuthal error could be due to heterogeneous viscosity within the eastern Tibetan Plateau. Exploration of such possibilities is beyond the scope of this study. It is also worth noting that the shallow afterslip distribution is anti-correlated with the coseismic rupture asperities (Fig. 4c) with peaks near where repeating earthquakes were observed during 2000–2008 (Li et al., 2011). Such identically repeating earthquakes are generally considered to represent repeated asperity failures driven by surrounding aseismic fault creep (Nadeau and McEvilly, 2004).

6.2. Heterogeneous rheology and the geodynamics of Tibet

Tomographic and receiver function studies (Li et al., 2009; Zhang et al., 2009b; Li et al., 2009) find a reduced shear wave velocity and higher Poisson's ratio in Tibet's lower crust, which may reflect fluids or elevated temperatures. Magnetotelluric resistivity measurements also suggest elevated fluid content in eastern Tibet's middle-to-lower crust (Zhao et al., 2012; Rippe and Unsworth, 2010). Additionally, the temperature is estimated to be >800 °C at >30 km depth below the Lhasa block in central Tibet (Mechie et al., 2004) and in southern Tibet (Wang et al., 2013), much higher than in the Sichuan Basin (~500 °C at 30 km depth, Wang, 2001). These thermal conditions suggest temperatures above the solidus of dry or wet granite while more mafic rock types that are likely to make up the lower crust of Tibet will deform by crystal plastic flow at these conditions (Klemperer, 2006). The Sichuan Basin, on the other hand, has a thick, high-velocity lithospheric root (Li and van der Hilst, 2010) and a low geothermal gradient (Wang, 2001).

The strongly asymmetric distribution of postseismic deformation observed following the 2008 Wenchuan earthquake reveals viscous relaxation in the lower crust of Tibet, whereas little if any deformation occurred in the cratonic lithospheric block underlying the Sichuan Basin. A weak and viscous ($\eta_M = 10^{18}$ Pa s) lower crust beneath the Tibetan Plateau that relaxes the coseismic stress changes can explain the middle- to far-field postseismic

displacements well (Figs. 3 and 4). In Fig. 6, we compare viscosity estimates for Tibetan lower crust obtained using different types of constraints, including postseismic deformation (10^{17}–10^{19} Pa s; Ryder et al., 2011; Wen et al., 2012; Zhang et al., 2009a; Yamasaki and Houseman, 2012; Ryder et al., 2010), GPS measurements of interseismic velocities (10^{18}–10^{19} Pa s; DeVries and Meade, 2013; Hilley et al., 2005, 2009), paleo-lake shoreline rebound (10^{19}–10^{20} Pa s; England et al., 2013), magnetotelluric resistivity data (10^{18}–10^{20} Pa s; Rippe and Unsworth, 2010), and geodynamic models (3×10^{17}–10^{21} Pa s; Beaumont et al., 2001; Clark et al., 2005; Cook and Royden, 2008), involving time scales of up to a few Ma. Most of the viscosity estimates span a wide range from 3×10^{17} to 3×10^{19} Pa s across all time scales, which includes the value found in this study. On the other hand, we find that little if any viscous relaxation occurred in the Sichuan Basin lithosphere following the Wenchuan earthquake (upper mantle $\eta_M > 10^{20}$ Pa s).

The lower crustal viscosity inferred by postseismic deformation studies is about three to five orders of magnitude lower than the inferred lithosphere-averaged viscosities found in geodynamic deformation models by England and Houseman (1985), England and Molnar (1997), Flesch et al. (2001), and Copley and McKenzie (2007). The main difference is that in postseismic studies, a depth dependent viscosity is necessary to produce reasonable near and far-field displacements in space and time, whereas the thin viscous sheet models of regional deformation assume a constant effective viscosity throughout the lithosphere, including the upper elastic crust that deforms by brittle faulting. Given these different model assumptions, these viscosity estimates should not be directly compared. Copley et al. (2011) use a two-layered viscosity structure in a model trying to explain the difference in tectonic deformation style between southern and northern Tibet by coupling to the underthrusting Indian crust. Their model requires a high-viscosity lower Tibetan crust (5×10^{23} Pa s) below southern Tibet, possibly due to an anhydrous, granulite lithology. This rheology structure and argument against channel flow below southern Tibet is inconsistent with our results from eastern Tibet.

A Maxwell fluid with a constant viscosity fails to explain the postseismic displacement rate changes, and shows the need of a model in which the effective viscosity increases with time. The change of effective viscosity implies either transient rheology or stress-dependent power-law rheology or both (Freed et al., 2012). In this study we try to distinguish the main mechanism that contributes to the postseismic displacements and the contrasting rheology between Tibet and Sichuan, and thus adopt a simple biviscous Burgers rheology. As the viscoelastic relaxation model can explain most of the early postseismic transients in the middle field, we can rule out afterslip as being the major cause of the initial rapid displacements.

Models of Tibetan lower crustal channel flow predict that the Plateau margins are steepest where the viscosity of the surrounding blocks are highest, and thus impede and divert the flow (Royden et al., 2008; Beaumont et al., 2001; Clark et al., 2005; Cook and Royden, 2008). These models predict the strongest viscosity contrasts with the Sichuan and Tarim Basin blocks ($\eta = 10^{16-18}$ Pa s in a 15–20 km thick lower crustal layer versus $\sim 10^{20-21}$ Pa s in adjacent crust), where topographic gradients are greatest. Our preferred viscosity structure deduced from the postseismic deformation transients across the Longmen Shan is consistent with such contrasting lithospheric rheology and deformation between eastern Tibet and the Sichuan Basin.

Acknowledgements

We thank D. Dreger, Z. Shen, I. Ryder, and F. Pollitz for discussions and constructive suggestions. Two anonymous reviewers give constructive comments on improving the manuscript. This project is supported by the National Science Foundation grant (EAR-1014880). This is Berkeley Seismological Laboratory contribution #14-1.

Appendix A. Supplementary information

Supplementary material related to this article can be found online at http://dx.doi.org/10.1016/j.epsl.2014.04.003.

References

Barbot, S., Hamiel, Y., Fialko, Y., 2008. Space geodetic investigation of the coseismic and postseismic deformation due to the 2003 M_w 7.2 Altai earthquake: implications for the local lithospheric rheology. J. Geophys. Res. 113, B03403.

Beaumont, C., et al., 2001. Himalayan tectonics explained extrusions of low-viscosity crustal channel coupled to focused surface denudation. Nature 414, 738–742.

Burchfiel, B.C., et al., 2008. A geological and geophysical context for the Wenchuan earthquake of 12 May 2008, Sichuan, People's Republic of China. GSA Today 18, 4–11.

Bürgmann, R., Dresen, G., 2008. Rheology of the Lower crust and upper mantle: evidence from rock mechanics, geodesy & field observations. Annu. Rev. Earth Planet. Sci. 36, 531–567.

Chen, C.W., Zebker, H.A., 2002. Phase unwrapping for large SAR interferograms: statistical segmentation and generalized network models. IEEE Trans. Geosci. Remote Sens. 40 (8), 1709–1719.

Chopra, P.N., 1997. High-temperature transient creep in olivine rocks. Tectonophysics 279, 93–111.

Clark, K.M., Bush, J.W.M., Royden, L.H., 2005. Dynamic topography produced by lower crustal flow against rheological strength heterogeneities bordering the Tibetan Plateau. Geophys. J. Int. 162, 575–590.

Cook, K., Royden, L.H., 2008. The role of crustal strength variations in shaping orogenic plateaus, with application to Tibet. J. Geophys. Res. 113, B08407.

Copley, A., Avouac, J.-P., Wernicke, B.P., 2011. Evidence for mechanical coupling and strong Indian lower crust beneath southern Tibet. Nature 472, 79–81.

Copley, A., McKenzie, D., 2007. Models of crustal flow in the India–Asia collision zone. Geophys. J. Int. 169, 683–698.

DeVries, P.M.R., Meade, B.J., 2013. Earthquake cycle deformation in the Tibetan plateau with a weak mid-crustal layer. J. Geophys. Res. 118, 3101–3111.

Ding, K., Xu, C., Wen, Y., 2013. Postseismic deformation associated with the 2008 Wenchuan earthquake by GPS data [in Chinese]. Geomat. Inf. Sci. Wuhan Univ. 38, 131–135.

England, P., Houseman, G., 1985. Role of lithospheric strength heterogeneities in the tectonics of Tibet and neighbouring regions. Nature 315, 297–301.

England, P., Molnar, P., 1997. Active deformation of Asia: from kinematics to dynamics. Science 278, 647–650.

England, P.C., Walker, R.T., Fu, B., Floyd, M.A., 2013. A bound on the viscosity of the Tibetan crust from the horizontality of paleolake shorelines. Earth Planet. Sci. Lett. 375, 44–56.

Flesch, L.M., Haines, A.J., Holt, W.E., 2001. The dynamics of the India–Eurasia collision zone. J. Geophys. Res. 106, 16,435–16,460.

Freed, A., Bürgmann, R., Calais, E., Freymueller, J., Hreinsdottir, S., 2006. Implications of deformation following the 2002 Denali, Alaska, earthquake for postseismic relaxation processes and lithospheric rheology. J. Geophys. Res. 111, B01401.

Freed, A., Hirth, G., Behn, M.D., 2012. Using short-term postseismic displacements to infer the ambient deformation conditions of the upper mantle. J. Geophys. Res. 117, B01409.

Guo, X., et al., 2013. Imaging the crustal structure beneath the eastern Tibetan Plateau and implications for the uplift of the Longmen Shan range. Earth Planet. Sci. Lett. 379, 72–80.

Hearn, E.H., 2003. What can GPS data tell us about the dynamics of post-seismic deformation? Geophys. J. Int. 155, 753–777.

Hilley, G.E., et al., 2005. Bayesian inference of plastosphere viscosities near the Kunlun Fault, northern Tibet. Geophys. Res. Lett. 32, L01302.

Hilley, G.E., et al., 2009. Earthquake-cycle deformation and fault slip rates in northern Tibet. Geology 37, 31–34.

Huang, M.-H., Dreger, D., Bürgmann, R., Yoo, S.-H., Hashimoto, M., 2013. Joint inversion of seismic and geodetic data for the source of the 2010 March 4, M_w 6.3 Jia-Shian, SW Taiwan, earthquake. Geophys. J. Int. 193, 1608–1626.

Hubbard, J., Shaw, J.H., Klinger, Y., 2010. Structural setting of the 2008 M_w 7.9 Wenchuan, China, earthquake. Bull. Seismol. Soc. Am. 100, 2713–2735.

Jia, D., et al., 2010. Structural model of 2008 M_w 7.9 Wenchuan earthquake in the rejuvenated Longmen Shan thrust belt, China. Tectonophysics 491, 174–184.

Johnson, K.M., Fukuda, J., Segall, P., 2012. Challenging the rate-state asperity model: afterslip following the 2011 M9 Tohoku-oki, Japan, earthquake. Geophys. Res. Lett. 39, L20302.

Jónsson, S., Segall, P., Pedersen, R., Björnsson, G., 2008. Post-earthquake ground movements correlated to pore-pressure transients. Nature 4242, 179–183.
Klemperer, S.L., 2006. Crustal flow in Tibet: geophysical evidence for the physical state of Tibetan lithosphere, and inferred patterns of active flow. In: Law, R.D., Searle, M.P., Godin, L. (Eds.), Channel Flow, Ductile Extrusion and Exhumation in Continental Collision Zones. In: Special Publications, vol. 268. Geological Society, London, pp. 39–70.
Li, L., Chen, Q.-F., Niu, F., Su, J., 2011. Deep slip rates along the Longmen Shan fault zone estimated from repeating microearthquakes. J. Geophys. Res. 116, B09310.
Li, H., Su, W., Wang, C.-Y., Huang, Z., 2009. Ambient noise Rayleigh wave tomography in western Sichuan and eastern Tibet. Earth Planet. Sci. Lett. 282, 201–211.
Li, C., van der Hilst, R.D., 2010. Structure of the upper mantle and transition zone beneath South East Asia from travel time tomography. J. Geophys. Res. 115, B07308.
Manning, C.E., Ingebritsen, S.E., 1999. Permeability of the continental crust: implications of geothermal data and metamorphic systems. Rev. Geophys. 37, 127–150.
Mechie, J., et al., 2004. Precise temperature estimation in the Tibetan crust from seismic detection of the α–β quartz transition. Geology 32, 601–604.
Nadeau, R.M., McEvilly, T.V., 2004. Periodic pulsing of characteristic microearthquakes on the San Andreas Fault. Science 303, 220–222.
Nelson, K.D., et al., 1996. Partially molten middle crust beneath southern Tibet; synthesis of Project INDEPTH results. Science 274, 1684–1688.
Peltzer, G., Rosen, P., Rogez, F., Hudnut, K., 1996. Postseismic rebound in fault stepovers caused by pore fluid flow. Science 273, 1202–1204.
Pollitz, F.F., 1992. Postseismic relaxation theory on the spherical Earth. Bull. Seismol. Soc. Am. 82, 422–453.
Pollitz, F.F., 2003. Transient rheology of the uppermost mantle beneath the Mojave Desert, California. Earth Planet. Sci. Lett. 215, 89–104.
Qi, W., et al., 2011. Rupture of deep faults in the 2008 Wenchuan earthquake and uplift of the Longmen Shan. Nat. Geosci. 4, 634–640.
Rippe, D., Unsworth, M., 2010. Quantifying crustal flow in Tibet with magnetotelluric data. Phys. Earth Planet. Inter. 179, 107–121.
Rosen, P.A., Hensley, S., Peltzer, G., 2004. Updated repeat orbit interferometry package released. EOS, Trans. Am. Geophys. Un. 85 (5), 35.
Royden, L.H., Burchfiel, B.C., van der Hilst, R., 2008. The geological evolution of the Tibetan Plateau. Science 321, 1054–1058.
Ryder, I., Bürgmann, R., Pollitz, F., 2011. Lower crustal relaxation beneath the Tibetan Plateau and Qaidam Basin following the 2001 Kokoxili earthquake. Geophys. J. Int. 187, 613–630.
Ryder, I., Bürgmann, R., Sun, J., 2010. Tandem afterslip on connected fault planes following the 2008 Nima-Gaize (Tibet) earthquake. J. Geophys. Res. 115, B03404.
Ryder, I., Parsons, B., Wright, T.J., Funning, G., 2007. Postseismic motion following the 1997 Manyi (Tibet) earthquake: InSAR observations and modeling. Geophys. J. Int. 169, 1009–1027.
Shao, Z., Wang, R., Wu, Y., Zhang, L., 2011. Rapid afterslip and short-term viscoelastic relaxation following the 2008 M_w 7.9 Wenchuan earthquake. Earthquake Sci. 24, 163–175.
Shen, Z.-K., Lu, J.N., Wang, M., Bürgmann, R., 2005. Contemporary crustal deformation around the southeast borderland of the Tibetan Plateau. J. Geophys. Res. 110, 11409.
Shen, Z.-K., et al., 2009. Slip maxima at fault junctions and rupturing of barriers during the 2008 Wenchuan earthquake. Nat. Geosci. 2, 718–724.
Tapponnier, P., et al., 2001. Oblique stepwise rise and growth of the Tibet plateau. Science 294, 1671–1677.
Thatcher, W., 2009. How the continents deform: the evidence from tectonic geodesy. Annu. Rev. Earth Planet. Sci. 37, 237–262.
Wang, Y., 2001. Heat flow pattern and lateral variations of lithosphere strength in China mainland: constraints on active deformation. Phys. Earth Planet. Inter. 126, 121–146.
Wang, R., Lorenzo-Martin, F., Roth, F., 2006. PSGRN/PSCMP-A new code for calculating co- and post-seismic deformation, geoid and gravity changes based on the viscoelastic-gravitational dislocation theory. Comput. Geosci. 32, 527–541.
Wang, K., Hu, Y., He, J., 2012. Deformation cycles of subduction earthquakes in a viscoelastic Earth. Nature 484, 327–332.
Wang, C.-Y., Chen, W.-P., Wang, L.-P., 2013. Temperature beneath Tibet. Earth Planet. Sci. Lett. 375, 326–337.
Wen, Y., Li, Z., Xu, C., Ryder, I., Bürgmann, R., 2012. Postseismic motion after the 2001 M_w 7.8 Kokoxili earthquake in Tibet observed by InSAR time series. J. Geophys. Res. 117, B08405.
Yamasaki, T., Houseman, G.A., 2012. The crustal viscosity gradient measured from post-seismic deformation: a case study of the 1997 Manyi (Tibet) earthquake. Earth Planet. Sci. Lett. 351, 105–114.
Zhang, C., Cao, J., Shi, Y., 2009a. Studying the viscosity of lower crust of Qinghai–Tibet Plateau according to post-seismic deformation. Sci. China 52 (3), 411–419.
Zhang, Z., et al., 2009b. Crustal structure across Longmenshan fault belt from passive source seismic profiling. Geophys. Res. Lett. 36, L17310.
Zhang, P.-Z., Wen, X.-Z., Shen, Z.-K., Chen, J.-H., 2010. Oblique high-angle, listric-reverse faulting and associated development of strain: the Wenchuan earthquake of May 12, 2008, Sichuan, China. Annu. Rev. Earth Planet. Sci. 38, 353–382.
Zhao, G., et al., 2012. Crustal structure and rheology of the Longmenshan and Wenchuan M_w 7.9 earthquake epicentral area from magnetotelluric data. Geology 40, 1139–1142.